

Semi-ionic Model for Metal Oxides and Their Interfaces with Organic Molecules

Lifeng Zhao, Lianchi Liu, and Huai Sun*

School of Chemistry and Chemical Technology, Shanghai Jiao Tong University, Shanghai 200240, China

Received: March 5, 2007; In Final Form: May 16, 2007

A semi-ionic model is proposed for simulations of bulk metal oxides and interfaces between metal oxides and organic molecules. In this model, the electrostatic interactions are represented by partial charges on atoms; the covalent contributions are represented by a Morse function, and the van der Waals interactions are represented by a Lennard-Jones (LJ) function. Four potential functions are parametrized, using experimental data of representative binary oxides, by combining the Morse and electrostatic terms with LJ-12-6, LJ-9-6, and polarization shell model. The resulting potential functions are validated by predicting bulk properties of binary and ternary oxides. Coupled with classical force field parameters for organic molecules, one of the potentials is applied to study the adsorption energies, structures, and isothermal curves of methanol molecules on a MgO (100) surface.

1. Introduction

There has been considerable interest in the development of potential models for metal oxides since the late 1970s.^{1–10} Among them is the ionic model, in which the formal charges of metal cations and oxygen anions are used in the Coulomb interaction terms are dominate. Coupled with short-range repulsive and long-range dispersion forces,^{11,12} with or without the shell model of Dick and Overhauser¹³ for describing the polarization effects, the ionic models perform well in the prediction of various bulk and surface properties of oxides. For examples, Lewis et al.³ reported good agreement with experimental data for lattice energies, diffusion activation energies, and elastic constants; Bush et al.⁷ applied the ionic model to predict properties of ternary oxides successfully. It has also been demonstrated that some modified ionic models can be applied to predict surface properties.^{14–16}

One of the areas of metal oxide research that receives the most interest is the inorganic–organic interfaces. For example, the painting or coating of materials on metal surfaces mostly involved molecular interactions with the metal oxides. Metal oxides are also common catalytic materials. Atomistic simulations of inorganic–organic interfaces require accurate description of the interatomic forces. However, the common force fields for organic materials are based on valence models in which partial charges on atoms are used. The inconsistency in the treatment of electrostatic interactions in the ionic and valence models made any attempts of combining the classical force fields for organic molecules with ionic potentials for metal oxides to represent the interfacial interactions unsuccessful. It is highly desirable to have a model that can be used not only to predict the bulk and surface properties of metal oxides but also to treat the interfaces of inorganic–organic interfaces.

It is well-known by quantum chemistry calculations that the covalent contributions are significant even in the most polar chemical bonds such as that in CH₃Li.¹⁷ A hybrid bond model, consisting of ionic and covalent contributions, is consistent with the physical picture. On the basis of this argument, we propose

a functional representation similar to that used for the organic materials for metal oxides. In this approach, the formal charges are replaced by partial charges. To compensate for the bonding energies, we use a Morse function to represent the covalent contribution. The primary objective is to make a potential model that is suitable not only for the bulk materials but also for the interfaces between the oxides and organic molecules.

In the following sections, we first present the functional forms and the parametrization procedure of our new model, and then we introduce the validation results obtained for bulk oxides. The validations include calculations on the training set of binary oxides and extended predictions for ternary oxides. Finally, we present a preliminary study of using one of our potential functions with the COMPASS force field¹⁸ to simulate the interactions of methanol molecules on the MgO (100) surfaces. It is demonstrated that the model can be used to predict the bulk properties of binary and ternary metal oxides in a similar quality as the ionic models. More importantly, this model can be combined with common force fields to represent the interfacial interactions between metal oxides and organic molecules.

2. Semi-Ionic Model

In this model, the electrostatic interactions are calculated using Coulomb law

$$V_{\text{elec}}(r) = \sum q_i q_j / r \quad (1)$$

where q_i are q_j are partial charges on interaction sites i and j , respectively. The interaction sites are usually the atomic nuclei but may be the electron shell sites in the shell model. For atoms that are directly bonded, this term represents the ionic contribution in the bond energies.

The covalent contributions of the metal–oxygen bonds are represented by a Morse function

$$V_{\text{M-O}}(r) = D_e \{ [1 - \exp(-\alpha(r - r_0))]^2 - 1 \} \quad (2)$$

For atoms that are not directly bonded, the Lennard-Jones function (LJ) is used to calculate the van der Waals energies.

* To whom correspondence should be addressed. E-mail: huaisun@sjtu.edu.cn. Tel: +86-21-5474-8987. Fax: +86-21-5474-1297.

TABLE 1: Metal Oxides with Their Lattice Types, Space Group Symbols, and NBO Partial Charges Calculated for the Cations

oxide	lattice	space group	q (M)
Na ₂ O	cubic	$Fm\bar{3}m$	0.586
MgO	cubic	$Fm\bar{3}m$	1.584
Al ₂ O ₃	hexagonal	$R\bar{3}c$	2.124
CaO	cubic	$Fm\bar{3}m$	1.510
TiO ₂	tetragonal	$I41/amd$	1.905
VO	cubic	$Fm\bar{3}m$	1.169
MnO	cubic	$Fm\bar{3}m$	0.988
FeO	cubic	$Fm\bar{3}m$	1.251
Fe ₂ O ₃	hexagonal	$R\bar{3}c$	1.611
CoO	cubic	$Fm\bar{3}m$	1.330
CuO	monoclinic	$C2/c$	1.263
ZnO	hexagonal	$P63mc$	1.534
SnO	tetragonal	$P4/nmm$	1.218

In this work, we employed both LJ-12-6 and LJ-9-6 functions. The LJ-12-6 function and its combination rules are given in the following equations:

$$V_{12-6}(r) = \epsilon_0((r_0/r)^{12} - 2(r_0/r)^6) \quad (3)$$

$$r_0 = (r_i + r_j)/2 \quad (4)$$

$$\epsilon_0 = \sqrt{\epsilon_i \epsilon_j} \quad (5)$$

The LJ-9-6 function and its 6-order combination rules are given as

$$V_{9-6}(r) = \epsilon_0(2(r_0/r)^9 - 3(r_0/r)^6) \quad (6)$$

$$r_0 = ((r_i^6 + r_j^6)/2)^{1/6} \quad (7)$$

$$\epsilon_0 = 2\sqrt{\epsilon_i \epsilon_j}(r_i^3 r_j^3 / (r_i^6 + r_j^6)) \quad (8)$$

The LJ function is used for metal-metal and oxygen-oxygen interactions. For metal-oxygen interactions, a Morse function that is switched off by eq 9 is used for directly bonded pairs.

$$f(r) = \frac{1}{1 + \exp(\eta(r - r_a))} \quad (9)$$

where the switching distance, r_a , is an adjustable parameter, between the first and second layers of the cation and anions.

The shell model is used to represent the polarization effects. In this model, only the oxygen atom is polarizable. The atomic polarizability is given by

$$\alpha = q_{\text{shell}}^2/k \quad (10)$$

where q_{shell} is the partial charge on the shell site and k is a harmonic spring constant that links the shell and the core charge sites.¹³ The core and shell charges are determined by splitting the total partial charge q_O on oxygen anion

$$\begin{aligned} q_{\text{core}} &= -0.5q_O \\ q_{\text{shell}} &= 1.5q_O \end{aligned} \quad (11)$$

Because the partial charges of the oxygen atoms are different in different oxides, the polarizabilities of the oxygen atoms are different in different oxides. However, the spring constant k is transferable; only one parameter is used for all oxides, and it is treated as an adjustable parameter to be optimized.

Thirteen metal oxide structures were used for the parametrization. These structures belong to four lattice types and six

different space groups. The lattice type and space group symbols are listed in Table 1.

Because the atomic partial charges are not measurable properties, there is no objective criterion for the derivation of “accurate” partial charges. Several options can be used to estimate the atomic partial charges. In this work, we used the natural bond orbital (NBO) analysis¹⁹ performed on cluster models of metal oxides to estimate the atomic partial charges. The cluster structures were taken from the super-cells of the oxide crystals and fixed. Each of the clusters contains at least 64 atoms so that the centers of the clusters approximately resemble the environment of the atoms in the solids. At the B3LYP/6-31G* level of theory, we calculated the NBO charges for the cations, and the values are given in Table 1. The charges of oxygen atoms are calculated using stoichiometry of the oxides. The quantum calculations were performed using the Gaussian03 software package.²⁰

With the partial charges fixed, we optimized the potential parameters by fitting the experimental data^{21,22} of the oxides. The experimental data include structural parameters, elastic constants, dielectric constants, and lattice energies. The unit-cell symmetry constraints were enforced in the fitting procedure. We carried out the parameter optimizations using the GULP program.^{23,24}

With the combination of two types of LJ functions, with and without the shell model, we parametrized four potential functions. The optimized potential parameters are given in Tables 2 and 3.

3. Results and Discussion

3.1. Validation on Bulk Properties of the Training Set. In Table 4, the lattice parameters and characteristic fractional coordinates of the binary oxides are given. The calculated data are based on the optimized structures using the potential energy functions. For comparison, the experimental data and the calculated results using the ionic models⁷ are listed in the table. Generally speaking, all of the computational results agree well with the experimental data. It should be noted that the semi-ionic models yield results similar to those of the ionic model, as indicated by the calculated root mean squares (rms) deviations listed in the last row of the table. In Table 5, the calculated lattice energies are compared with the experimental values. Excellent agreements between the calculated and experimental data are obtained. Again, all four sets of potential functions proposed in this paper yield similarly good results; the rms deviations from the experimental data are less than 0.002 eV.

The shell model is critical in the representation of the dielectric properties, especially for the high-frequency values. With the charges fixed from ab initio calculations, the only parameter that can be adjusted for the shell model is the spring constant k of the oxygen shell model. The optimized value, as given in Table 2, is 34.46 eV/Å.² This parameter leads to a reasonably good fit of the reported relative dielectric constants,²⁵⁻³⁰ as given in Table 6.

We also obtained good agreement between the calculated and experimental data for the elastic constants of the oxide crystals, as shown in Figure 1. The elastic constants are sensitive to the curvatures of the potential surfaces. It appears that the LJ-12-6 function performs slightly better than the LJ-9-6 function, with and without the shell model.

Generally speaking, the potentials proposed perform well for the prediction of the properties of bulk binary oxides. It is of interest to note that the fit quality is related to the symmetric

TABLE 2: Optimized Morse Parameters of the Cation–Oxygen Interaction Terms^a

cations	parameters	LJ-9–6		LJ-12–6		cutoff
		no shell	shell	no shell	shell	
Na(I)	De	1.949352	1.879959	1.960831	1.847134	3.0
	α	0.661370	0.943830	0.653578	0.904721	
	r_0	2.579	2.543	2.584	2.579	
Mg(II)	De	1.934739	1.868331	1.951349	1.926396	2.8
	α	0.885203	0.836525	0.881293	0.855299	
	r_0	2.525	2.620	2.525	2.566	
Al(III)	De	6.380	6.435352	6.467	6.434711	2.5
	α	0.835211	0.875568	0.758221	0.75627	
	r_0	2.192	2.197	2.228	2.226123	
Ca(II)	De	2.107386	1.959012	2.150862	2.087932	3.0
	α	0.768513	0.571171	0.765653	0.568917	
	r_0	2.815	3.437	2.814	3.387	
Ti(IV)	De	13.57049	13.58151	13.66022	13.62392	3.0
	α	0.605801	0.611617	0.557993	0.567675	
	r_0	2.065	2.057	2.057	2.081198	
V(II)	De	4.252830	4.245068	4.223554	4.262390	2.8
	α	0.561366	0.562259	0.521930	0.538777	
	r_0	2.180	2.179	2.280	2.225936	
Mn(II)	De	4.567486	4.235028	4.606009	4.376867	3.0
	α	0.491398	0.403363	0.475590	0.400746	
	r_0	2.249	2.681	2.272	2.623	
Fe(II)	De	3.654137	3.637717	3.669842	3.637717	2.8
	α	0.620924	0.621504	0.601307	0.621504	
	r_0	2.350	2.350	2.385	2.350	
Fe(III)	De	8.467283	8.502043	8.408777	8.379944	2.8
	α	0.456788	0.399347	0.495903	0.518692	
	r_0	2.423	2.451	2.352	2.333	
Co(II)	De	3.366740	3.349396	3.380716	3.376772	2.8
	α	0.666951	0.661580	0.645206	0.645586	
	r_0	2.366	2.380	2.408	2.403	
Cu(II)	De	6.595517	5.868191	6.550403	6.059232	3.0
	α	3.745831	11.71051	3.782068	10.81111	
	r_0	1.940	1.957	1.948	2.005	
Zn(II)	De	3.492523	3.471444	3.496166	3.504734	2.8
	α	0.818065	0.758922	0.792243	0.752662	
	r_0	2.353	2.397	2.386	2.409	
Sn(II)	De	1.122263	1.061054	1.274160	1.275236	3.0
	α	2.803922	1.745162	2.365859	1.572601	
	r_0	2.007	2.114	2.018	2.217	

^a The spring constants of oxygen shells in both 9–6 and 12–6 models are 34.46 eV/Å². The units of the parameters are De in eV, α in Å⁻¹, and r_0 in Å.

level of the lattice unit cells. For instance, with the LJ-12–6 model, the rms is 0.008 for the cubic structures, 0.019 for the hexagonal ($R\bar{3}C$) structure of Al₂O₃, and 0.075 for Fe₂O₃. This may be associated with the inadequateness of the isotropic potential functions. Among the oxides studied in this work, two worst fits are found for SnO ($P4/nmm$) and CuO ($C2/c$). In SnO, the most significant deviation is the position (fractional coordinate) of the tin atom, with a percentage deviation of 17.9%. On the basis of our best knowledge, the SnO has not been parametrized previously so that we do not have a direct comparison to evaluate the proposed semi-ionic model. Islam et al. published a potential for CuO.³¹ The rms of the structures predicted by their potential is 0.357, which is greater than the value (0.160) we have obtained.

3.2. Validation on Transferability: Properties of Ternary Oxides. To extend the calculations to oxides outside of the training set a critical test for the potential functions was presented. To explore the capability of the semi-ionic models, we calculated properties of several ternary oxides by using the derived parameters without any modification.

First we optimized the unit cell structures of MgAl₂O₄,³² TiMn₂O₄,³³ ZnAl₂O₄,³⁴ ZnFe₂O₄³⁵ (spinel, $Fd\bar{3}m$ symmetry), CaTiO₃ (perovskite, $Pbnm$ symmetry),³⁶ FeTiO₃ (ilmenite, $R\bar{3}c$ symmetry),³⁷ and FeCuO₂ (delafossite, $R\bar{3}m$ symmetry).³⁸ In

TABLE 3: Optimized Nonbond Lennard-Jones Potential Parameters for Metal Oxides^a

cations	parameters	9–6		12–6	
		no-shell	shell	no-shell	shell
Na(I)	ϵ	0.012540	0.045038	0.005641	0.095598
	σ	3.438	2.925	3.438	2.760
Mg(II)	ϵ	0.007887	0.161058	0.000854	0.068751
	σ	3.402	2.891	3.402	2.566
Al(III)	ϵ	0.000786	0.000377	0.000930	0.021315
	σ	3.521	1.856	2.273	2.898
Ca(II)	ϵ	0.063317	0.975952	0.042375	0.883907
	σ	3.507	3.18761	3.378	3.179
Ti(IV)	ϵ	0.003941	0.000637	0.002700	0.056157
	σ	4.250	5.237	4.201	3.523
V(II)	ϵ	0.023366	0.023413	0.037165	0.010851
	σ	3.695	3.680	3.306	3.601
Mn(II)	ϵ	0.045189	0.315881	0.020207	0.221641
	σ	3.800	3.276	3.800	3.246
Fe(II)	ϵ	0.018580	0.019584	0.008091	0.019584
	σ	3.950	3.900	3.906	3.900
Fe(III)	ϵ	0.021490	0.001528	0.000012	0.000741
	σ	4.077	5.268	5.996	2.664
Co(II)	ϵ	0.013871	0.021051	0.006935	0.0077984
	σ	3.960	3.810	3.840	3.818
Cu(II)	ϵ	0.122261	0.000584	0.100254	0.000578
	σ	3.980	5.452	3.826	4.968
Zn(II)	ϵ	0.000162	0.006764	0.000063	0.000380
	σ	6.327	4.393	5.822	5.079
Sn(II)	ϵ	0.120330	0.043087	0.037080	0.044100
	σ	4.310	4.553	4.404	4.531
O(II)	ϵ	0.003400	0.003400	0.003400	0.003400
	σ	3.627	3.627	3.627	3.627

^a The units are ϵ in eV and σ in Å.

these calculations, the partial charges of the cations were taken from the binary systems directly. The charges of oxygen atoms were calculated by balancing the total charge using the stoichiometry of the ternary oxides.

Table 7 lists the structural data obtained using the semi-ionic potentials and the ionic model published in references.^{3,7,8} The experimental data are listed for comparisons. Overall, the semi-ionic models yield good agreement with the experimental data. Although the total rms deviations of the semi-ionic models are slightly higher than the ionic models, the problems are from FeCuO₂, in which the potential parameters for Cu²⁺ is likely problematic as discussed above. The rms deviations, excluding the FeCuO₂ results, of the four semi-ionic models are all less than 0.2, at the same level of the ionic models.

A further test was carried out by calculation of the compressibility of the ternary structure of ZnAl₂O₄. We carried out NPT ensemble molecular dynamics to estimate the density this material at 300 K and in the pressure range from 0 to 42.9 GPa. The NPT simulations were performed with the Nose–Hoover method for temperature control and the Parrinello method for pressure control. The time step of the simulations was 1 fs. Each of the simulated systems was equilibrated for 10 000 steps, followed by a 50 000 steps for data production. The average unit-cell edge parameters are displayed in Figure 2, together with the experimental data and calculated data in ref 34 for comparison.

The calculated results, under 10 GPa, using all semi-ionic potentials agree very well with the experimental data. The errors are roughly $\pm 0.1\%$. Among them, the potentials with LJ-9–6 function perform slightly better than those with the LJ-12–6 function. The potentials with LJ-12–6 function underestimate the values if coupled with the shell model (LJ-12–6-s) and overestimate the values without the shell model (LJ-12–6). However, the potentials with the LJ-9–6 function fails to

TABLE 4: Comparison of the Structural Properties of Oxide Crystals^a

oxide	lattice parameter	exptl	calculated ^b					Bush
			12-6-n	12-6-s	9-6-n	9-6-s		
Na2O	<i>a</i>	5.550	5.549	5.550	5.547	5.549	5.550	
MgO	<i>a</i>	4.211	4.211	4.208	4.204	4.211	4.206	
Al2O3	<i>a</i>	4.759	4.797	4.784	4.844	4.864	4.820	
	<i>c</i>	12.991	12.997	12.956	12.874	12.924	13.012	
	<i>x</i> (O)	0.306	0.308	0.308	0.297	0.298	0.296	
	<i>z</i> (Al)	0.352	0.355	0.355	0.354	0.354	0.356	
CaO	<i>a</i>	4.798	4.798	4.797	4.798	4.798	4.793	
TiO2	<i>a</i>	3.776	3.664	3.701	3.607	3.617	3.624	
	<i>c</i>	9.486	9.482	9.475	9.480	9.511	9.587	
	<i>x</i> (O)	0.208	0.211	0.212	0.203	0.205	0.198	
VO	<i>a</i>	4.080	4.082	4.080	4.082	4.082		
Mn	<i>a</i>	4.445	4.445	4.443	4.445	4.443		
FeO	<i>a</i>	4.332	4.332	4.332	4.332	4.332		
Fe2O3	<i>a</i>	5.035	5.096	5.069	5.032	2.218	5.047	
Fe2O3	<i>c</i>	13.720	13.690	13.699	13.658	13.736	13.562	
Fe2O3	<i>x</i> (O)	0.300	0.308	0.307	0.305	0.336	0.295	
Fe2O3	<i>z</i> (Fe)	0.355	0.358	0.355	0.365	0.376	0.355	
CoO	<i>a</i>	4.267	4.267	4.267	4.267	4.267		
CuO	<i>a</i>	4.653	4.958	4.963	4.928	4.850		
CuO	<i>b</i>	3.410	3.411	3.400	3.425	3.312		
CuO	<i>c</i>	5.108	5.012	5.167	4.966	5.037		
CuO	β	1.737	1.736	1.729	1.736	1.732		
ZnO	<i>a</i>	3.249	3.274	3.262	3.274	3.260		
ZnO	<i>c</i>	5.205	5.185	5.187	5.187	5.188		
ZnO	<i>z</i> (O)	0.383	0.387	0.387	0.386	0.387		
SnO	<i>a</i>	3.796	3.875	4.167	3.836	3.934		
SnO	<i>c</i>	4.836	4.836	4.869	4.791	4.757		
SnO	<i>z</i> (Sn)	0.236	0.193	0.199	0.200	0.191		
rms			0.068	0.094	0.085	0.066	0.067	

^a The calculated data include semi-ionic models (this work) and ionic model (Bush, ref 7). Characteristic fractional coordinates are listed for low-symmetry oxides. The root-mean-square deviations between the calculated and experimental values are given for overall comparison. The experimental data are taken from refs 23 and 24. The lengths are in angstroms (Å), and the angles are in radians. ^b 12-6-n, 12-6-s, 9-6-n, and 9-6-s denote potential models with LJ-12-6 function, LJ-12-6 with oxygen shell function, LJ-9-6 function, LJ-9-6 function with oxygen shell model, respectively.

TABLE 5: Comparison of the Lattice Sublimation Energies (in eV) of the Metal Oxides^a

oxide	exptl	calculated			
		12-6-n	12-6-s	9-6-n	9-6-s
Na ₂ O	25.71	25.71	25.71	25.74	25.71
MgO	39.29	39.29	39.29	39.29	39.30
Al ₂ O ₃	329.92	329.91	329.89	325.87	329.92
CaO	35.38	35.38	35.38	35.38	35.37
TiO ₂	225.53	225.88	225.81	225.86	225.83
VO	41.66	41.66	41.66	41.49	41.66
MnO	38.37	38.38	38.38	38.38	38.38
FeO	39.33	39.33	39.33	39.33	39.33
Fe ₂ O ₃	296.61	296.61	296.62	296.48	296.53
CoO	40.01	40.01	40.01	40.01	40.01
CuO	83.95	85.41	84.05	85.50	84.05
ZnO	79.33	79.33	79.32	79.32	79.32
SnO	37.85	37.85	37.85	37.85	37.56
rms ($\times 100$)		0.125	0.009	0.142	0.015

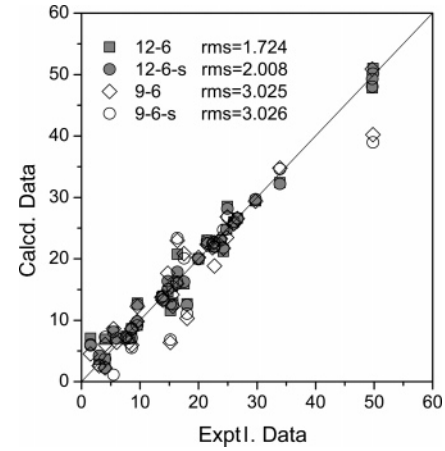
^a The calculations are done using four semi-ionic potential functions. The root mean square (rms) deviations between the calculated and experimental data are listed. The experimental data are taken from refs 23 and 24.

maintain the crystalline structure as the pressure increases to ~ 14.0 GPa with the shell model. This problem did not show up if the shell model is excluded. In fact, the potentials with the shell model generally perform worse than those without the

TABLE 6: Comparison of the Calculated and Experimental Relative Dielectric Constants^a

oxide	component	exptl	9-6-s	12-6-s
Al ₂ O ₃	ϵ_0^{11}	9.385	3.757	7.022
	ϵ_0^{33}	11.614	4.091	7.361
	ϵ_∞^{11}	3.077	2.536	2.957
	ϵ_∞^{33}	3.072	2.556	2.930
CaO	ϵ_0^{11}	12	12.009	11.915
	ϵ_∞^{11}	3.35	2.125	2.124
MgO	ϵ_0^{11}	9.87	9.175	9.428
	ϵ_∞^{11}	2.96	2.039	2.948
MnO	ϵ_0^{11}	20.89	20.892	20.891
	ϵ_∞^{11}	4.95	1.574	1.574
ZnO	ϵ_0^{11}	7.77	7.322	7.291
	ϵ_0^{33}	8.91	9.064	9.094
	ϵ_∞^{11}	3.7	2.321	2.319
	ϵ_∞^{33}	3.78	2.342	2.341

^a The calculations were performed with two semi-ionic shell models. The experimental data are taken from refs 25–30.

**Figure 1.** Comparison of the calculated (calcd) and experimental (exptl) elastic constants (at 10 GPa).

shell model. Presumably the additional flexibility introduced by the shell model causes the overall instability in the potential functions.

For comparison, we also applied the potential parameters made by Binks et al.³⁹ and Lewis et al.³ in the calculations. With the Binks model, we could not obtain a stable crystal structure, the model is unstable in the constant pressure simulations. With the Lewis potential, we obtained stable results only under 3.1 GPa. However, the Lewis model underestimated the cell edge parameters with large errors.

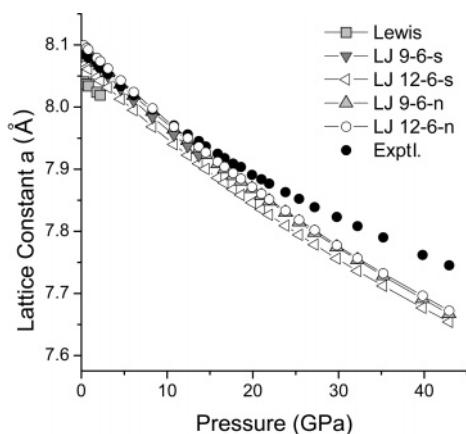
As the pressure increases, the deviations between the calculated and experimental data increase in general. The calculated cell edge parameters are systematically too low, which means the predicted densities are too high. This indicates the role of repulsion in the potential function, mostly the Morse functions between the cations and anions, may be too soft. Further investigation is required to fully understand and solve this problem.

3.3. Methanol Adsorption on the Magnesium Oxide Surface. As a classical model system, methanol adsorption on the MgO surface has been studied by several research groups using various experimental methods.^{40–44} Three types of species have been identified on the MgO surfaces: methanol physisorbed to the substrate, methanol “chemisorbed” to the substrate

TABLE 7: Comparison of Predicted and Experimental Data of Structural Parameters of Ternary Metal Oxides^a

compounds	lattice parameters	exptl	semi-ionic model (this work)				ionic model		
			12-6-n	12-6-s	9-6-n	9-6-s	Lewis	Bush	Woodley
MgAl ₂ O ₄	<i>a</i> (Å)	8.0844	8.1206	8.0831	8.1051	8.1847	7.7934	8.136	8.0782
TiMn ₂ O ₄	<i>a</i>	8.6789	8.4902	8.6074	8.4878	8.6074	8.6851		
ZnAl ₂ O ₄	<i>a</i>	8.0912	8.0938	8.0644	8.0691	8.0915	7.8837		
	<i>x</i> (O)	0.2638	0.2637	0.2654	0.2649	0.2647	0.2705		
ZnFe ₂ O ₄	<i>a</i>	8.4412	8.4748	8.3758	8.7940	8.6523	8.0970		
CaTiO ₃	<i>a</i>	5.4043	5.3010	5.4921	5.2616	5.7028	5.4843	5.2984	
	<i>b</i>	5.4224	5.3010	5.4922	5.2616	5.7028	5.4950	5.2984	
	<i>c</i>	7.6510	7.4966	7.7671	7.4409	8.0650	7.7675	7.4930	
	<i>x</i> (Ca)	0.9916	0.9630	0.9630	0.9630	0.9630	0.9820	0.9630	
	<i>y</i> (Ca)	0.0123	0.0380	0.0380	0.0380	0.0380	0.0231	0.0380	
	<i>x</i> (O)	1.0586	0.9630	0.9630	0.9630	0.9630	0.0252	0.9630	
	<i>y</i> (O)	0.4687	0.537998	0.5380	0.538002	0.5380	0.5131	0.538	
FeTiO ₃	<i>a</i>	5.1233	4.993323	5.0778	5.041124	4.9813			5.038131
	<i>c</i>	13.7602	13.79507	13.5973	13.57206	13.6388			13.36075
	<i>z</i> (Fe)	0.3554	0.372256	0.3725	0.379285	0.3712			0.370927
	<i>z</i> (Ti)	0.1464	0.155574	0.1493	0.157273	0.1538			0.157374
FeCuO ₂	<i>a</i>	3.0278	3.417467	3.4038	3.456433	3.2816			
	<i>c</i>	17.0936	18.17436	18.9520	18.07059	18.3606			
rms			0.2830	0.4519	0.2837	0.3431	0.1513	0.1361	0.1829

^a The predicted data were calculated using four semi-ionic models (this work) and ionic model (from literature). The experimental data are taken from refs 32–38 (lengths in Å).

**Figure 2.** Comparison of calculated and experimental lattice constants of ZnAl₂O₄ as functions of pressure.

through a hydrogen bond to the oxygen anion in the surface, and methanol dissociated and its fragments chemisorbed to the substrate.⁴³ It is generally accepted that the bond dissociations only occur on defect-rich sites.^{43,45} Using volumetric adsorption isotherms and neutron diffraction spectra, Trabelsi et al.⁴⁴ suggested two layers of methanol placed on the MgO (100) surface and a subdivision of the two layers at lower temperature. Despite the great interest in this system and ample experimental data reported in the literature, theoretical approaches have been limited to quantum mechanics calculations of small cluster models.^{45,46}

The methanol adsorption on the MgO surfaces without bond dissociation presents an excellent test case for the potential functions presented in this paper. Assuming the interactions between a methanol molecule and the substrate can be represented by nonbond interactions only, we applied the force field simulation methods to study the interfacial phenomenon of methanol molecules on the MgO (100) surfaces.

The surface is represented by a 3-D slab model that mimics the thin film prepared experimentally.⁴² The slab is cleaved on the (100) surface with a thickness of ~ 13.0 Å along the *z* direction. The slab is $\sim 25 \times 25$ (Å²) in the *x* and *y* directions. A 40 Å vacuum is placed on top of the slab so that the entire system is a 3-D box. The simulation box is subject to the

TABLE 8: Comparison of Structural Properties Predicted for Methanol Molecule Adsorbed on the MgO (1 0 0) Surface Using the Derived Potential Energy Function with Those Obtained from Small Cluster Models⁴² Using the HF/6-31G(d,p) Method^a

	H _p ...O ²⁻	O...Mg ²⁺	H _p -O	O-C	∠H _p -O-C
this work	1.464	2.706	0.999	1.417	105.98
HF/6-31G(d,p) ⁴²	1.877	3.245	0.955	1.417	110.4

^a The bond lengths are in angstroms, and the bond angles are in degrees.

periodic boundary condition in calculations. The COMPASS force field¹⁸ is used for the methanol molecule, the semi-ionic model with LJ-9-6 function is used for the MgO. The interactions between the MgO and methanol are only the LJ and the electrostatic terms. The simulations were conducted using the TOWHEE Monte Carlo package.⁴⁷

First we estimated the binding energy of methanol on the MgO surface by placing one methanol molecule on the surface. Taking a series configurations generated by the Monte Carlo simulations, we calculated the average adsorption energy by subtracting the total energy of the model by the sum of the energy of methanol molecule in gas phase and the energy of the MgO slab. The value obtained is 18.1 kcal/mol, in good agreement with the value (17.4 kcal/mol) derived from the TPD measurements.⁴² In comparison, the adsorption energies predicted using small molecular clusters are ~ 9 kcal/mol at the HF level and 13.8 kcal/mol at the MP2 level.^{45,46} The predicted structural data are compared with the HF/6-31G(d,p) results⁴⁶ in Table 8. The most significant difference is in the distance of the hydrogen bond formed between the methanol hydroxyl hydrogen and the oxide oxygen. Our potential predicts significantly shorter distance (1.464 Å) than that (1.877 Å) obtained using the HF/6-31G(d) method. The hydrogen bond distance is shorter than the normal hydrogen bond lengths (~ 1.8 – 2.2 Å), but it is consistent with the extremely strong binding energy. We argue that this hydrogen bond is very different from normal hydrogen bonds, as classified as chemisorbed in the literature.

Next we applied the constant pressure Gibbs ensemble Monte Carlo (CP-GEMC) method^{48,49} to predict the adsorption isotherms of methanol molecules on the MgO surfaces. Two

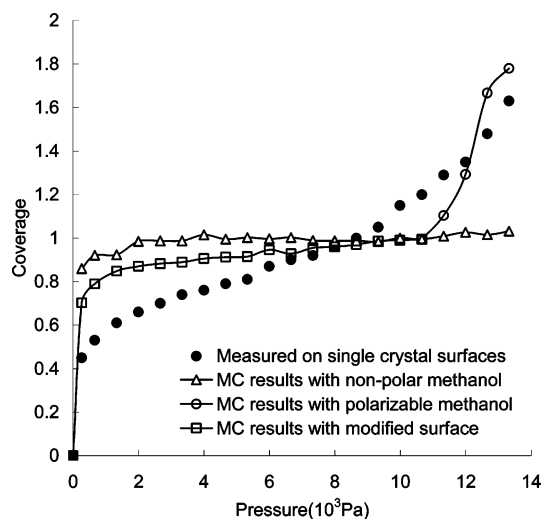


Figure 3. Comparison of isotherm curves of methanol on MgO (100) surfaces at room temperature (300 K). The calculations were performed on defect-free or modified surfaces; the experimental curves were measured on single-crystal surface.⁴⁰

simulation boxes with 3-D periodic boundary condition were simulated in parallel; one represents the surface region, another represents the gas phase of methanol. Three types of MC moves were performed in the simulations: the change of volume of the gas phase, translation and rotation of methanol molecules in each of the two phases, and transfer of a methanol molecule between the two phases. The last move was performed using the configuration-biased growth method.⁴⁷ The simulation was carried out for at least 50 million moves for the equilibration of the system and 50 million moves for data production. The simulation was conducted at 300K, with the vapor pressure of the methanol ranging from 0 to 0.014 MPa (the saturated vapor pressure).

The adsorption curve obtained is presented in Figure 3. The coverage is calculated by division of the number of molecules in the surface box by the number of anion on the surface. The adsorption starts as soon as a pressure is imposed, reflecting the relatively strong interfacial interaction (18.1 kcal/mol). The coverage curve increases rapidly as the vapor pressure increases, and it reaches complete coverage (1.0) of the surface at pressure around 2.6×10^{-4} MPa. Elevated pressures do not change the coverage in the pressure range calculated. The sharp increase of coverage at low pressure has been observed by Trabelsi et al. who reported the surface would be covered with a monolayer of methanol molecules at 2–8 Pa at 300 K.⁴⁴ However, this result is significantly different from that reported based on spectroscopic measurements on single crystals in which the full coverage does not occur until 8000 Pa.⁴⁰ This may be the result of the different experimental conditions and substrates used. Although the surface structures were not explicitly discussed in the references, it is likely the surfaces are not the same. Nevertheless, a comparison with the experimental isotherms is beneficial for understanding the interactions on the surfaces. Since the pressure range considered is convenient for simulations, we mainly compare our results with that reported in ref 40. As shown in Figure 3, the calculated isotherm diverges from the measured significantly. In the low-pressure region, the experimental curve increases much slower than the calculated. At the high-pressure end (0.011–0.014 MPa), the experimental adsorption curve continues to increase, while the calculated curve does not.

The difference in low-pressure range is readily explained by the fact that the atomistic models are not comparable between

the calculations and the experiments.⁴⁰ On the basis of our calculations and the experimental work on the MgO/Mo thin film,⁴² the interaction of methanol and the surface is fairly strong (17–18 kcal/mol), exclusively, via the methanol–surface hydrogen bonds. In the single-crystal measurements, the surface interactions are more complex; it is deduced that the methanol molecules interact with the surface and with each other on the surface.⁴⁰ The hydrogen bonds among the methanol molecules are much weaker than the hydrogen bonds between methanol and the anions on the surface. If the surfaces are covered by methoxyl or hydroxyl groups, the interfacial interactions between the methanol molecules and the modified surfaces would be weakened; consequently, the isotherm should show strong pressure dependence.

To verify this point, we constructed a hypothetical surface by randomly saturating 75% anions on the surface by hydrogen atoms. The hydrogen atoms are assigned to a positive charge of 0.4 e, and the additional charges were neutralized by subtracting the charges on cations. Other force field parameters were unchanged. As expected, the adsorption curve obtained with the modified surface demonstrates the pressure dependence, as shown in Figure 3. The isotherm curve with the modified surface moves toward the experimental one. More interestingly, the monolayer coverage is reached at about 9.3×10^{-3} MPa, consistent with the experimental observation.

At the pressures from 0.011 to 0.014 MPa, it appears additional molecules are too weak to be bonded to the monolayer-covered surface. The interaction terms between an adsorbent molecule and the covered surface include contributions from the substrate and adsorbed methanol molecules. Assuming the underestimate of interaction strength is the result of those from adsorbed methanol molecules, we deduce that the neglect of the polarization effect on the methanol molecules in classical force field is the cause of the discrepancy. With the charge models for metal oxides used in this work, the electric fields above the MgO surface with a distance of 3.0 and 6.0 Å (approximate distances of the first and second layers of methanol molecule on the MgO surface respectively) are about 2.6×10^9 and 2.0×10^8 V/m, respectively. With the average polarizability of 3.3 Å^3 of the methanol molecule,²¹ the induced dipole moments are about 0.30 Debye for the first layer and 0.02 Debye for the second layer. The additional energy contributions from the induced dipoles are not negligible for the first layer.

To test this argument, we scaled the atomic partial charges of methanol molecules on the surfaces to fit the total dipole moments of the methanol molecules in the first layer. With this modification, the predicted adsorption curve increases significantly at the high-pressure region (0.011–0.014 MPa), which qualitatively agree with the experimental data, as shown in Figure 3.

A snapshot of the generated configurations at the pressure of 0.0127 MPa is shown in Figure 4. It clearly demonstrates a tightly bonded first layer of methanol molecules on the surface. Each of the methanol molecules is bonded to the surface via a hydrogen bond between the hydroxyl group and the oxygen anion. Beyond the first layer, the molecules are randomly distributed. From the top view of the surface (Figure 5), one sees that each hydrogen atom of methanol is pointed toward an oxygen atom on the surface. However, the directions of the methyl groups of methanol are random. This is in contrast with deductions made based on the experimental work.^{40,42,44} From the thermodynamic point of view, the oxygen atom in MgO is more polarized than that in the methanol; consequently, it is a

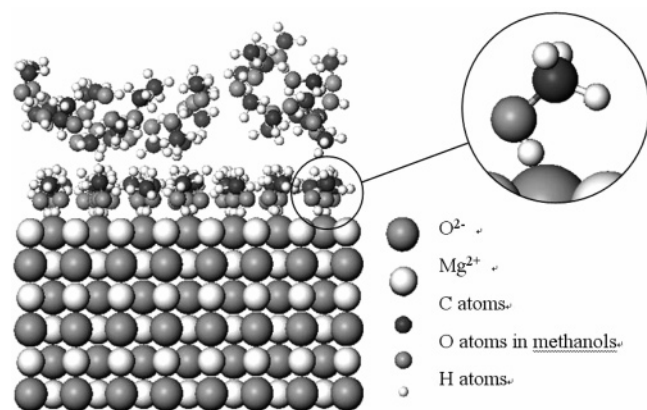


Figure 4. Snapshot of the interface configuration generated by MC simulation. The methanol molecules are bonded to the surface by strong hydrogen bonds between the hydroxy hydrogen and oxygen anions.

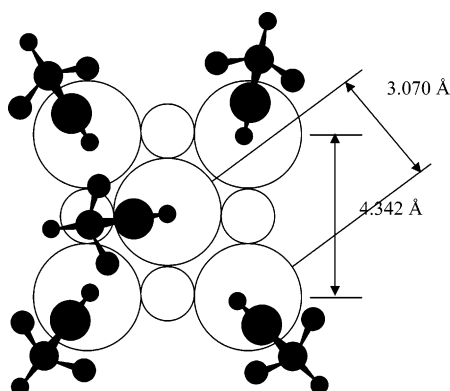


Figure 5. Schematic representation of one-layer methanol adsorbed on MgO(100) surface. The small and large empty circles correspond to Mg and O surface atoms, respectively.

stronger hydrogen-bond acceptor. By formation of hydrogen bonds with the surface, the system gains lower total enthalpy. The random orientation of methyl groups leads to higher entropy of the system.

An analysis of the energies provides more information on the nature of the adsorption. As we have discussed above, the adsorption energy of one methanol on the bare MgO surface is 18.1 kcal/mol. When the surface has adsorbents, the interactions become more complicated. We examined this issue from different angles: After the first layer is completely covered and the polarization is added to the first layer, the binding energy of a molecule to the surface is about 8.2 kcal/mol, which is much lower than that obtained for the first layer. Removal of the polarization lowers this energy to 6.9 kcal/mol. From the completely covered and polarized surface, it costs ~ 11.1 kcal/mol to remove the central molecule in Figure 5. This indicates the intermolecular interaction between the central and surrounding molecules is repulsive in nature. However, to further remove another molecule on the cell vertex needs 22.4 kcal/mol, indicating the intermolecular interaction is attractive in this case.

The energetic data can be readily explained by the geometric feature of the unit cell of MgO. As shown in Figure 5, two oxygen atoms along the cell edge is placed at a distance of 4.342 Å, which allows enough space for the attached methanol molecules and in general the interactions between methanol molecules are attractive. The distance of two methanol molecules along the diagonal line in the unit cell is 3.07 Å, which leads to strong repulsion between the methyl groups.

Finally we point out that the central molecule is relatively unstable. The structure showing in Figure 5 is a snapshot taken

at lower temperature (230 K). At elevated temperature (300 K), this molecule escapes from the first layer. This probably reflects the observed subdivision of the adsorption isotherms reported in the literature.⁴⁴ In addition, we propose the energy released (11.1 kcal/mol) may correspond to the second type adsorption energy of 14.8 kcal/mol reported in reference.⁴²

4. Conclusions

In this paper, we report a semi-ionic model for metal oxides and their interfaces with organic molecules. We call it semi-ionic because the chemical bonds between the cations and anions are represented by both electrostatic and covalent terms. By combining LJ-12-6 and LJ-9-6 functions with and without the polarization shell model, we parametrized four potential energy functions. Validations of these potential functions yield excellent agreement with experimental data for structural properties, lattice energies, dielectric constants, and elastic constants for 13 binary oxides. More importantly, these potential functions work well for predicting bulk properties of ternary systems without any modifications on the potential parameters. The calculation of the compressibility of a ternary metal oxide in a broad range of pressures indicates the model could be applied to predict other thermodynamic properties.

In comparison with previous models proposed for metal oxides, the present model uses partial charges instead of formal charges in the Coulombic term. The use of partial charges has a couple of consequences. Although the partial charges cannot be rigorously defined, a rough estimate of the partial charges leads to a clear differential of the covalent and ionic contributions in polar chemical bonds, which resembles the physical reality that can be revealed using quantum mechanics calculations. The partial charges are determined by the chemical compositions and structures. Not only the cations (metal or transition metal atoms) but also the anions (oxygen atoms) have different charge values in different oxides. If these atoms are considered to be different “atom types”, this phenomenon is consistent with that in the classical force fields. The transferability of the charge parameters is valid when the local environments for those atoms are similar, as we have demonstrated in this work by moving the charge parameters from the binary to ternary oxides. It should be noted that only one parameter, the spring constant k , is used in the shell model for the oxygen anions.

Since the semi-ionic model is consistent with the classical force fields, it can be applied together with common force fields to represent the interactions between metal oxides and organic molecules. Similar to other force field applications, this approach is valid only for systems that do not involve bond dissociations. In this work, we studied the methanol adsorption on the MgO (100) surfaces by combining one of the potential functions (LJ-9-6) with the COMPASS force field. The estimated adsorption energy (~ 18.1 kcal/mol) and structures of methanol molecules on the defect-free surface agrees well with the experimental data.⁴² In addition, a close examination of the microscopic structures of the adsorbed molecules illustrated a rather complex interaction pattern. The first layer molecules are bonded to the surface exclusively via extremely strong hydrogen bonds. Intermolecular forces among adsorbents are weak van der Waals in nature and could be repulsive and attractive depending on the sites on the surface. Direct comparison of the calculated adsorption isotherms with experimental data is complicated by many factors; among them, the most important one is likely the surface structure. The force field could be improved as well. As explained, the interactions between the methanol molecules

and methanol-covered surfaces appear to be underestimated using the classical force fields. This reveals the importance of including polarization of the organic molecules in the classical force field. By building realistic and accurate potential energy functions, we started to tackle the correlations between the surface structures and adsorption isotherms in this work.

Acknowledgment. Financial support from the National Science Foundation of China (NSFC, No. 20473052) for the development of force field method is gratefully acknowledged.

References and Notes

- (1) Catlow, C. R. A. *Proc. R. Soc. London, Ser. A* **1977**, 333, 533.
- (2) Sanders, M. J.; Leslie, M. J.; Catlow, C. R. A. *J. Chem. Soc., Chem. Commun.* **1984**, 1271.
- (3) Lewis, G. V.; Catlow, C. R. A. *J. Phys. C: Solid State Phys.* **1985**, 18, 1149.
- (4) Jackson, R. A.; Catlow, C. R. A. *Mol. Simul.* **1988**, 1, 207.
- (5) van Beest, B. W. H.; Kramer, G. J.; van Santen, R. A. *Phys. Rev. Lett.* **1990**, 64, 1955.
- (6) Jentys, A.; Catlow, C. R. A. *Catal. Lett.* **1993**, 22, 251.
- (7) Bush, T. S.; Gale, J. D.; Catlow, C. R. A.; Battle, P. D. *J. Mater. Chem.* **1994**, 4, 831.
- (8) Woodley, S. M.; Battle, P. D.; Gale, J. D.; Catlow, C. R. A. *Phys. Chem. Chem. Phys.* **1999**, 1, 2535.
- (9) Sastre, G.; Gale, J. D. *Chem. Mater.* **2003**, 15, 1788.
- (10) Schroder, K. P.; Sauer, J.; Leslie, M.; Catlow, C. R. A.; Thomas, J. M. *Chem. Phys. Lett.* **1992**, 188, 320.
- (11) Baram, P. S.; Parker, S. C. *Philos. Mag. B* **1996**, 73, 49.
- (12) Kerisit, S.; Parker, S. C. *J. Am. Chem. Soc.* **2004**, 126, 10152.
- (13) Dick, B. G.; Overhauser, A. W. *Phys. Rev.* **1958**, 112, 90.
- (14) Soetens, J. C.; Millot, C.; Hoang, P. N. M.; Girardet, C. *Surf. Sci.* **1998**, 419, 48.
- (15) Maureen, I. M.; Gregory, K. S.; Carol, A. S.; John, B. N. *J. Phys. Chem.* **1996**, 100, 16989.
- (16) Bandura, A. V.; Kubicki, J. D. *J. Phys. Chem. B* **2003**, 107, 11072.
- (17) Matthias, B.; Nicolaas, J. R.; van Eikema, H. C.; Fonseca, G.; Evert, J. B. *Organometallics* **1996**, 15, 2923.
- (18) Sun, H. J. *J. Phys. Chem. B* **1998**, 102, 7338.
- (19) Larry, A. Curtiss; Frank, Weinhold, *Chem. Rev.* **1988**, 88, 899.
- (20) Frisch, M. J.; Trucks, G. W.; Schlegel, H. B.; Scuseria, G. E.; Robb, M. A.; Cheeseman, J. R.; Montgomery, J. A., Jr.; Vreven, T.; Kudin, K. N.; Burant, J. C.; Millam, J. M.; Iyengar, S. S.; Tomasi, J.; Barone, V.; Mennucci, B.; Cossi, M.; Scalmani, G.; Rega, N.; Petersson, G. A.; Nakatsuji, H.; Hada, M.; Ehara, M.; Toyota, K.; Fukuda, R.; Hasegawa, J.; Ishida, M.; Nakajima, T.; Honda, Y.; Kitao, O.; Nakai, H.; Klene, M.; Li, X.; Knox, J. E.; Hratchian, H. P.; Cross, J. B.; Bakken, V.; Adamo, C.; Jaramillo, J.; Gomperts, R.; Stratmann, R. E.; Yazyev, O.; Austin, A. J.; Cammi, R.; Pomelli, C.; Ochterski, J. W.; Ayala, P. Y.; Morokuma, K.; Voth, G. A.; Salvador, P.; Dannenberg, J. J.; Zakrzewski, V. G.; Dapprich, S.; Daniels, A. D.; Strain, M. C.; Farkas, O.; Malick, D. K.; Rabuck, A. D.; Raghavachari, K.; Foresman, J. B.; Ortiz, J. V.; Cui, Q.; Baboul, A. G.; Clifford, S.; Cioslowski, J.; Stefanov, B. B.; Liu, G.; Liashenko, A.; Piskorz, P.; Komaromi, I.; Martin, R. L.; Fox, D. J.; Keith, T.; Al-Laham, M. A.; Peng, C. Y.; Nanayakkara, A.; Challacombe, M.; Gill, P. M. W.; Johnson, B.; Chen, W.; Wong, M. W.; Gonzalez, C.; Pople, J. A. *Gaussian 03*, revision A.1; Gaussian, Inc.: Pittsburgh, PA, 2003.
- (21) David, R. L. *CRC Handbook of Chemistry and Physics*, 75th ed.; CRC Press: London, 1994.
- (22) Samsonov, G. V. *The Oxide Handbook*; IFI/PLENUM: New York, 1973.
- (23) Gale, J. D. *J. Chem. Soc., Faraday Trans.* **1997**, 93, 629.
- (24) Gale, J. D.; Rohl, A. L. *Mol. Simul.* **2003**, 29, 291.
- (25) Schubert, M.; Tiwald, T. E.; Herzinger, C. M. *Phys. Rev. B* **2000**, 61 (12), 8187–8191.
- (26) Bartels, R. A.; Koo, J. C.; Thomas, M. L. *Phys. Status Solidi A* **1979**, 52 (2), K213–K216.
- (27) Eric, J. Wu; Gerbrand, Ceder *J. Appl. Phys.* **2001**, 89 (10), 5630–5636.
- (28) Umari, P.; Alfredo, Pasquarello *Phys. Rev. Lett.* **2002**, 89 (15), 157602–5.
- (29) David, Reagor; Fernando, Garzon *Appl. Phys. Lett.* **1991**, 58 (24), 2741–2743.
- (30) Shosuke, Mochizuki *J. Phys.: Condens. Matter* **1989**, 1, 10351–10359.
- (31) Islam, M. S.; Winch, L. *J. Phys. Rev. B* **1995**, 52, 10510.
- (32) Peterson, R. C.; Lager, G. A.; Hitterman, R. L. *Am. Mineral.* **1991**, 76, 1455.
- (33) Hugh, St. C. O.; Simon, A. T. R.; Sue, K.; Simine, S. *Am. Mineral.* **2003**, 88, 860.
- (34) Levy, D.; Pavese, A.; Sani, A.; Pischedda, V. *Phys. Chem. Miner.* **2001**, 28, 612.
- (35) Levy, D.; Pavese, A.; Hanfland, M. *Phys. Chem. Miner.* **2000**, 27, 638.
- (36) Takamitsu, Y.; Noriyuki, H.; Yutaka, K. *Am. Mineral.* **2002**, 87, 1183.
- (37) Leinenweber, K.; Linton, J.; Navrotsky, A.; Fei, Y.; Parise, J. B. *Phys. Chem. Miner.* **1995**, 22, 251.
- (38) Pabst, A. *Am. Mineral.* **1946**, 31, 539.
- (39) Binks, D. Jason; Grimes, Robin W. *Solid State Commun.* **1994**, 89, 921.
- (40) Jennifer, Rudberg; Michelle, Foster *J. Phys. Chem. B* **2004**, 108, 18311.
- (41) Liang, S. H.; Gay, I. D. *Langmuir* **1985**, 1, 593–599.
- (42) Günster, J.; Liu, G.; Stultz, J.; Krischok, S.; Goodman, D. W. *J. Phys. Chem. B* **2000**, 104, 5738–5743.
- (43) Cristiana, D. Valentin; Annalisa, D. Vito; Gianfranco, P.; Stéphane, Abbet; Anke, S. Wörz; Ken, Judai; Ueli, Heiz *J. Phys. Chem. B* **2002**, 106, 11961–11969.
- (44) Trabelsi, M.; Saidi, S.; Chefi, C.; Martin, C.; Lucas, S.; Ferry, D.; Suzanne J. *Surf. Sci.* **2004**, 566–568, 789–793.
- (45) Branda, M. M.; Ferullo, P. G. Belevi; Castellani, N. J. *Surf. Sci.* **2003**, 527, 89–99.
- (46) Branda, M. M.; Peralta, J. E.; Castellani, N. J.; Contreras, R. H. *Surf. Sci.* **2002**, 504, 235–243.
- (47) Martin, M. G.; Siepmann, J. I. *J. Phys. Chem. B* **1999**, 103, 4508.
- (48) Panagiotopoulos, A. Z.; Quirke, N.; Stapleton, M.; Tildesley, D. J. *Mol. Phys.* **1988**, 63, 527.
- (49) Simon, C. McGrother; Keith, E. Gubbins *Mol. Phys.* **1999**, 97, 955.